THE JOURNAL OF PHYSICAL CHEMISTRY C

Article

pubs.acs.org/JPCC

# Observation of Ferroelectricity and Structure-Dependent Magnetic Behavior in Novel One-Dimensional Motifs of Pure, Crystalline Yttrium Manganese Oxides

Jonathan M. Patete,[†] Jinkyu Han,[‡] Amanda L. Tiano,[†] Haiqing Liu,[†] Myung-Geun Han,[‡] J. W. Simonson,[§] Yuanyuan Li,[∥] Alexander C. Santulli,[†] M. C. Aronson,[‡,§] Anatoly I. Frenkel,[∥] Yimei Zhu,[‡] and Stanislaus S. Wong*[,†,‡]

[†]Department of Chemistry, State University of New York at Stony Brook, Stony Brook, New York 11794-3400, United States

[‡]Condensed Matter Physics and Materials Science Department, Building 480, Brookhaven National Laboratory, Upton, New York 11973, United States

[§]Department of Physics and Astronomy, State University of New York at Stony Brook, Stony Brook, New York 11794-3800, United States

[∥]Department of Physics, Yeshiva University, New York, New York 10016, United States

Supporting Information

**ABSTRACT:** Multiferroic materials, such as nanostructured *h*-$YMnO_3$, are expected to fulfill a crucial role as active components of technological devices, particularly for information storage. Herein, we report on the template mediated sol−gel synthesis of unique one-dimensional nanostructured motifs of hexagonal phase $YMnO_3$, possessing a space group of $P6_3cm$. We found that the inherent morphology of the as-obtained *h*-$YMnO_3$ nanostructures was directly impacted by the chemical composition of the employed membrane. Specifically, the use of anodic alumina and polycarbonate templates promoted nanotube and nanowire formation, respectively. Isolated polycrystalline nanotubes and single crystalline nanowires possessed diameters of 276 ± 52 nm, composed of 17 nm particulate constituent grains, and 125 ± 21 nm, respectively, with lengths of up to several microns. The structures and compositions of all our as-prepared products were probed by XRD, SEM, HRTEM, EXAFS, XANES, SAED, and far-IR spectroscopy. In the specific case of nanowires, we determined that the growth direction was mainly along the *c*-axis and that discrete, individual structures gave rise to expected ferroelectric behavior. Overall, our $YMnO_3$ samples evinced the onset of a spin-glass transition at 41 ± 1 K for both templateless bulk control and nanowire samples but at 26 ± 3 K for nanotubes. Interestingly, only the as-synthesized crystalline nanotubular mesh gave rise to noticeably enhanced magnetic properties (i.e., a higher magnetic moment of 3.0 $\mu_B$/Mn) as well as a lower spin-glass transition temperature, attributable to a smaller constituent crystallite size. Therefore, this work not only demonstrates our ability to generate viable one-dimensional nanostructures of a significant and commercially relevant metal oxide but also contributes to an understanding of structure−property correlations in these systems.

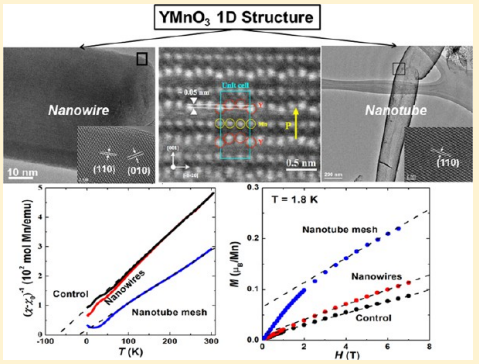


## 1. INTRODUCTION

Multiferroics are of technological interest because a selective property of the material can be either altered or tuned by independent variations of a distinct, yet correlated parameter. More specifically, these systems exhibit uniquely coupled magnetic and electric long-range ordering parameters and may also possess coupled ferroelasticity, as in the case of piezoelectrics.[1] This feature has led many to suggest that multiferroic materials will play an important role in engineering future devices for magnetoelectronic applications such as sensors, spintronics, and data storage.[2,3] Hence, there is much interest in the reliable synthesis of multiferroic materials with precise control over their size, shape, and composition.

Key examples of single phase multiferroics of interest include not only perovskite metal oxides such as $BiMnO_3$, $Pb(Zr,Ti)O_3$, $FeTiO_3$, and notably $BiFeO_3$ but also a number of hexagonal phase rare-earth manganites, which exhibit favorable magnetoelectric coupling.[1,4−6] Of this latter family of materials, the hexagonal phase of yttrium manganese oxide (*h*-$YMnO_3$) is a ferroelectric antiferromagnet at room temperature and offers significant potential in information storage technology.[2,3,7,8] Specifically, *h*-$YMnO_3$ possesses a unipolar axis along the [001] direction[9] and exhibits a relatively high ferroelectric transition

Received: July 9, 2014
Revised: August 22, 2014
Published: September 5, 2014

  

temperature ($T_C \approx 914$ K) as well as a comparatively low antiferromagnetic spin-ordering temperature ($T_N \approx 80$ K).[10] These characteristic properties, coupled with a fairly low dielectric constant[11] ($\varepsilon \sim 20$) and the material's intrinsic nonvolatile nature, render $YMnO_3$ as an excellent candidate for magnetoelectric sensors as well as for metal–ferroelectric–semiconductor field effect transistors (i.e., MFSFETs) in the next generation of media storage devices.[2,7]

It is important to note that while $YMnO_3$ possesses two stable crystallographic phases, namely orthorhombic and hexagonal phases, only the hexagonal structure exhibits ferroelectric ordering which arises from a geometrically strained state. Specifically, the structure of *h*-$YMnO_3$ (space group $P6_3cm$) consists of alternating layers of $Y^{3+}$ ions and manganese oxide trigonal bipyramids.[12] A slight tilting of the $MnO_5$ bipyramids below the Curie temperature ($T_C$) displaces the $Y^{3+}$ ions along the *c*-axis, giving rise to the observed ferroelectric properties of $YMnO_3$.[13−15] Further investigations with Raman and infrared spectroscopy were employed to probe the conversion from the paraelectric to ferroelectric phases at about $T_C$, confirming that the electronic transition arises from a geometrically induced structural distortion.[16−18] To summarize, the many interesting magnetic, electronic, and optical properties of $YMnO_3$ are a direct function of its unique crystallographic structure.[15,19,20]

Several methods have been employed to fabricate homogeneous thin films and polycrystalline ceramic powders of $YMnO_3$. These physicochemical methods include pulsed laser deposition, chemical solution deposition, metal–organic chemical vapor deposition, RF sputtering, molecular beam epitaxy, spark plasma sintering, autocombustion, solid-state reduction, and sol–gel techniques.[2,7,20−25] Whereas the preparation of thin films has been studied extensively, there are a limited number of existing reports regarding the synthesis of zero-dimensional (0D) nanoparticles and, in particular, one-dimensional (1D) nanostructures, implicitly suggesting challenges associated with their synthesis as pure crystalline materials.

Indeed, one-dimensional nanomaterials, such as nanotubes and nanowires, are highly sought after due to their inherent anisotropic nature, high surface area, and their ability to be easily incorporated into devices. Thus far, an extensive review of the literature indicates that $YMnO_3$ nanofibers have only been produced by a sol–gel-based electrospinning technique.[20] Although the morphology of these amorphous as-spun fibers was smooth and straight, the phase-pure crystalline product exhibited roughened external surfaces with diameters ranging between 200 and 800 nm as a result of the high annealing temperature used. Moreover, products annealed below 1100 °C contained sizable quantities of both yttrium oxide ($Y_2O_3$) and manganese oxide ($Mn_3O_4$) impurities.

Herein, we report on a relatively straightforward template-mediated sol–gel synthesis for one-dimensional structural motifs of $YMnO_3$, namely nanowires and a nanotubular mesh. Specifically, a colloidal sol is loaded into and subsequently infuses the pores of a commercial template. The idea is that the sol saturates the hollow channels of the template pores and the subsequent gelation reaction results in the formation of 1D products that more or less accurately mimic the intrinsic internal shape and imperfections of the spatially confining cylindrical channels themselves.[4,26] The distinctive advantage of using a template-based method is that the morphology of the product is specifically controlled by the spatial dimensions of the template, yielding a homogeneous, morphologically pure sample. As such, the diameters of the nanostructures can be readily tuned by varying the actual pore dimensions associated with the originating template.

Our results highlight that we are able to routinely synthesize pure, crystalline $YMnO_3$ 1D structures, consistent with a single hexagonal phase possessing a space group of $P6_3cm$. This is a significant finding, because in the case of individual nanowires, our data also provide clear evidence of ferroelectric ordering (Figure 4), which, to the best of our knowledge, has not been previously shown in such structural motifs. Moreover, we had initially hypothesized that the inherent morphology of the range of diverse $YMnO_3$ nanostructures analyzed dictates and correlates with magnetic behavior. By contrast, in this work, our results demonstrate that it is actually the intrinsic constituent crystallite size of the various $YMnO_3$ samples tested, which fundamentally governs the resulting magnetic behavior evinced by the material.

## 2. EXPERIMENTAL SECTION

**2.1. Preparation of 1D Nanostructures.** To prepare the precursor sol, yttrium(III) nitrate hexahydrate (Alfa Aesar, 99.9%), manganese(II) nitrate hydrate (Alfa Aesar, 99.98%), and anhydrous citric acid (Acros, 99.6%) were combined in a 1:1:2 molar ratio and then dissolved in 5 mL of anhydrous ethanol (Acros Organic, 99.5%) under sonication. In this system, citric acid plays the role of a chelating agent.[27,28] After sonication, the color of the sol is a light golden brown.

Nanowires were subsequently synthesized within a commercial polycarbonate (PC) track-etched membrane (Whatman) with nanosized cylindrical pores placed into a filter holder attached to a syringe. The sol was infused throughout the PC membrane channels with the manual assistance of a syringe pump. The loaded polycarbonate membrane was then dried for 1 h at 80 °C in order to induce gelation of the sol within the pores. Sol material remaining on the external surfaces of the template was removed by polishing the template on an Arkansas Wet-Stone (Tools for Working Wood Company, Brooklyn, NY). The amorphous product was isolated by dissolving the PC membrane in methylene chloride (Acros, 99.5%) followed by annealing in a muffle furnace at 800 °C for 2 h, thereby yielding individual *h*-$YMnO_3$ nanowires. We should clearly note that with this specific sol–gel precursor, individual crystalline yttrium manganate nanostructures could not be obtained at temperatures below 800 °C, i.e., even at 700 or 750 °C. Therefore, we were required to isolate the amorphous products prior to the final annealing step. Since the size and shape of the nanowires correspond to the dimensions of the originating template, the diameters of the nanowires can be reliably varied by altering the corresponding diameters of the channels within the PC template.

In this work, we will present nanowires prepared only from templates with pore diameters of ∼200 nm. The actual nanowire diameters are somewhat lower, presumably due to the physical inhomogeneity of the pore spaces as well as to structural contraction during the annealing step. For magnetic and electronic property comparisons, a templateless bulk control sample was also prepared in an identical fashion by annealing the sol in a porcelain boat, without loading it into a template.

Nanotubes were analogously obtained by filtering the same sol through a 200 nm pore size anodic alumina (AAO) template (Whatman) using a traditional vacuum filtration


dx.doi.org/10.1021/jp5068582 | J. Phys. Chem. C 2014, 118, 21695−21705

setup, with the assistance of a diffusion pump as the vacuum source. The loaded AAO template was subsequently dried at 80 °C for 1 h and then heated in a muffle furnace at 650 °C for 2 h in order to calcine the nanotubes. Residual sol material was removed from the external surfaces of the template by the polishing step previously described. Because AAO crystallizes into its difficult-to-remove corundum phase above 650 °C, the *h*-$YMnO_3$ product could not be further annealed without first isolating the amorphous nanotubes. Therefore, the AAO template was dissolved in 5 M NaOH (Mallinckrodt, 99.9%) with stirring to yield the amorphous yttrium manganate material. This as-obtained product was then placed into a porcelain-coated ceramic boat prior to annealing at 800 °C for 2 h to yield a crystalline *h*-$YMnO_3$ nanotubular mesh. In all cases, the product was removed from the porcelain boat by sonication in distilled water, subsequently washed during centrifugation steps, and ultimately dispersed in ethanol.

**2.2. Characterization.** To investigate the size and morphology of our as-prepared samples, the product was dispersed in ethanol, sonicated, drop-cast onto a clean silicon wafer, and characterized with either a Hitachi S-4800 field-emission scanning electron microscope (FE-SEM) operating at an accelerating voltage of 5 kV or a Leo 1550 FE-SEM operating at 20 kV with the capability of energy dispersive X-ray spectroscopy (EDS). The same preparation technique was also used to deposit samples onto a lacey carbon-coated copper grid for investigation with a FEI Tecnai12 BioTwinG$^2$ transmission electron microscope (TEM), equipped with an AMT XR-60 CCD digital camera system. High-resolution TEM (HRTEM) selected area electron diffraction (SAED) data were obtained with a JEOL 3000F (300 kV) microscope with a field emission gun (FEG). High-angle annular dark-field (HAADF) scanning TEM (STEM) was performed using a double-aberration corrected JEOL ARM-200CF (200 kV) with a cold FEG. The range of detection angles used for HAADF STEM imaging was from 68 to 280 mrad.

The crystallinity of the products was determined using both HRTEM and powder X-ray diffraction (XRD). To obtain XRD patterns, a concentrated slurry of the product, dispersed in ethanol, was sonicated and subsequently deposited onto an amorphous glass microscope slide, so that the ethanol would evaporate, thereby forming a homogeneous film of the as-prepared product. Diffraction patterns were obtained on a Rigaku Ultima III Diffractometer, operating in the Bragg configuration using Cu K$\alpha$ radiation (1.54 Å), and spanning a range from 25 to 60°, measured at a scanning rate of 1° per minute.

At the National Synchrotron Light Source, Mn K-edge data were collected at the X19A beamline and Y K-edge data were collected at the X18A beamline with both sets of measurements obtained in transmission mode. Different parameters contributing to the theoretical EXAFS equation (e.g., bond distances and energy origin correction or coordination numbers and the bond length disorder parameters) correlate in the fit. Constraining them during the fit improves the stability of the results. In our analysis, we modeled the Mn and Y K-edge data concurrently by applying multiple constraints. Only Mn−O, Mn−Mn, Mn−Y (two types) and Y−O, Y−Mn (two types) and Y−Y contributions to Mn and Y EXAFS data, respectively, were considered. The Mn−Y and Y−Mn bond length disorder parameters were constrained to be the same as measured from either edge.

In order to study the magnetic properties of $YMnO_3$ nanostructures, we measured both the temperature and field dependence of dc magnetization at a range from 1.8 to 300 K and in magnetic fields as large as 7 T, using a Quantum Design Magnetic Property Measurement System (MPMS-XL7) instrument. In a typical experiment, ∼5 mg of nanostructures was contained in gelatin capsules and fastened in plastic straws for immersion into the magnetometer. Field-dependent measurements were performed at 1.8 K, while the temperature dependence was measured at 1000 Oe. No subtraction of the diamagnetic signal associated with the sample container was made for the magnetization data.

Optical absorption in the far-infrared (far-IR) region was measured for the as-prepared yttrium manganese oxide samples using a Nexus 670 FT-IR (Thermo Nicolet) instrument, equipped with a single-reflectance zinc selenide (ZnSe) attenuated total reflectance (ATR) accessory, a solid substrate beam splitter, and a DTGS polyethylene detector. These as-prepared solid powders were placed onto the ZnSe crystal, and measurements were obtained in transmittance mode using the Smart Performer module. The data shown represent an average of 64 accumulated spectra.

## 3. RESULTS AND DISCUSSION

**3.1. Structural Characterization of 1D Nanomaterials.** The XRD patterns of our as-prepared bulk control, nanowire, and nanotube samples of $YMnO_3$ can be reliably assigned to the reflection of a single hexagonal phase possessing a space group of $P6_3cm$, an assertion which agrees well with the JCPDS # 72-3594, as shown in Figure 1. The crystallite sizes calculated from the Debye−Scherrer formula were found to be ∼14, 37, and 39 nm for nanotubes, nanowires, and bulk control samples of $YMnO_3$, respectively.

It should be mentioned that $YMnO_3$ maintains three crystalline polymorphs: i.e., two hexagonal structures with space groups of $P6_3/cm$ and $P6_3/mmc$ as well as one orthorhombic structure with a space group of *Pnma*. The

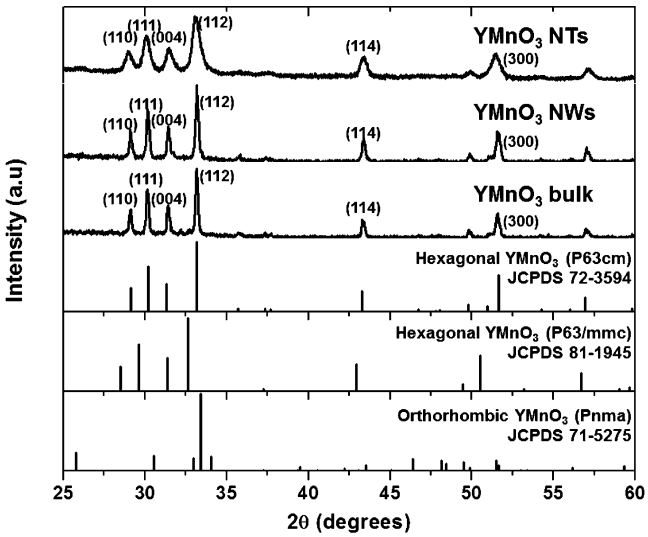


**Figure 1.** X-ray diffraction patterns obtained for our templateless bulk, nanowire, and nanotube $YMnO_3$ samples and the corresponding database standards for the three polymorphs of $YMnO_3$: JCPDS No. 72-3594 (hexagonal space group: $P6_3cm$), No. 81-1945 (hexagonal space group: $P6_{3/m}mc$), and No. 71-5275 (orthorhombic space group: *Pnma*).


dx.doi.org/10.1021/jp5068582 | J. Phys. Chem. C 2014, 118, 21695−21705

**Table 1. Interatomic Distances (in Å) between the Nearest Neighbors to Mn and Y in $YMnO_3$, Calculated Based on Prior Crystallographic Data (COD # 2011821) and Obtained Based on EXAFS Analysis of the Three Measured Materials, i.e., $YMnO_3$ Nanotubes, Nanowires, and Bulk Control Samples[a]**

| system | Mn−O(5) | Mn−Y1(3) | Mn−Mn(6) | Mn−Y2(3) | Y−O(7) | Y−Mn1(3) | Y−Y(6) | Y−Mn2(3) |
|---|---|---|---|---|---|---|---|---|
| $YMnO_3$ reference | [1.863, 2.062] | [3.286, 3.351] | [3.532, 3.549] | [3.666, 3.747] | [2.268, 2.432] | [3.286, 3.351] | [3.538, 3.570] | [3.666, 3.747] |
| bulk | 1.87 ± 0.02 | 3.28 ± 0.02 | 3.38 ± 0.05 | 3.69 ± 0.02 | 2.29 ± 0.01 | 3.33 ± 0.02 | 3.57 ± 0.01 | 3.73 ± 0.05 |
| nanowire | 1.87 ± 0.02 | 3.30 ± 0.05 | 3.45 ± 0.07 | 3.69 ± 0.05 | 2.30 ± 0.02 | 3.29 ± 0.04 | 3.57 ± 0.01 | 3.85 ± 0.07 |
| nanotube | 1.88 ± 0.02 | 3.30 ± 0.02 | 3.39 ± 0.05 | 3.69 ± 0.02 | 2.29 ± 0.02 | 3.33 ± 0.04 | 3.57 ± 0.03 | 3.72 ± 0.09 |

[a]The numbers in parentheses are the corresponding bond coordination numbers, which are fixed for all samples in fitting process. The numbers in square brackets indicate a range of distances for their respective atomic pairs.

orthorhombic and hexagonal polymorphs of $YMnO_3$ are similar in terms of Gibbs free energy, and therefore, the formation of these phases is highly dependent upon the relevant synthesis conditions and protocols.[29−32] Nonetheless, it is the hexagonal structure $YMnO_3$ with a space group of $P6_3cm$ that possesses superior multiferroic properties as compared with other polymorphs, due to its unique inherent crystal structure.[12,33,34]

Specifically, (a) the Y ion, coordinated with seven oxygen atoms and situated between layers of $MnO_5$ trigonal bipyramids, and (b) the Mn ions, surrounded by three in-plane and two apical oxygen atoms, form a triangular-lattice layer configuration, alternating with a Y ion layer, as shown in Figure S1. Triangular antiferromagnetic arrangements of $Mn^{3+}$ ions in the *ab*-plane can potentially induce noncentrosymmetric $Y^{3+}$ displacements, thereby producing spontaneous electric polarization along the *c*-axis.[12,33,34]

In order to further probe the crystal structure and determine the valence state of Mn in our $YMnO_3$ structure, X-ray absorption spectra including X-ray absorption near edge structure (XANES) and extended X-ray absorption fine structure (EXAFS) were collected. The interatomic distances which were extracted from EXAFS spectra have been summarized in Table 1 and Table S1. In Table 1, the bulk fit agrees with the $YMnO_3$ reference, with the exception of the Mn−Mn distances whose determination is complicated due to the superposition of Mn−Mn and two groups of Mn−Y pairs in the same distance range. The local structure in nanotubes appears to be very similar to that of the templateless bulk control sample; the nanowires differ in terms of the amount of disorder in Y−Mn pairs. In support of our XRD data, these interatomic distances for each of the elemental pairs appeared to be consistent with the hexagonal phase of $YMnO_3$, possessing a space group of $P6_3cm$.

Furthermore, the valence of Mn in the samples was estimated and calculated through the use of XANES spectra (Figure 2 as well as Figures S2 and S3). The determination of the valence states of Mn mainly relies on the (a) peak maximum and (b) corresponding energy value when the normalized absorption coefficient $\mu(E)$ reaches 0.5, which is also known as the 0.5 level.[35,36] It is evident that the nanowire sample possesses a charge state close to +3, as evidenced by both the peak maximum and the 0.5 level position. The bulk control and the nanotubes possess somewhat smaller than +3 in charge, as they are shifted toward lower energies as compared with the nanowire sample. Hence, they are denoted by $+3-\delta$. We can conclude therefore that the formal oxidation state of Mn in our all three samples is either effectively or very close to +3. Hence, it can be inferred that the crystal structure is not significantly dependent upon the actual morphology of $YMnO_3$ (e.g., nanowires versus nanotubes versus bulk control samples) and

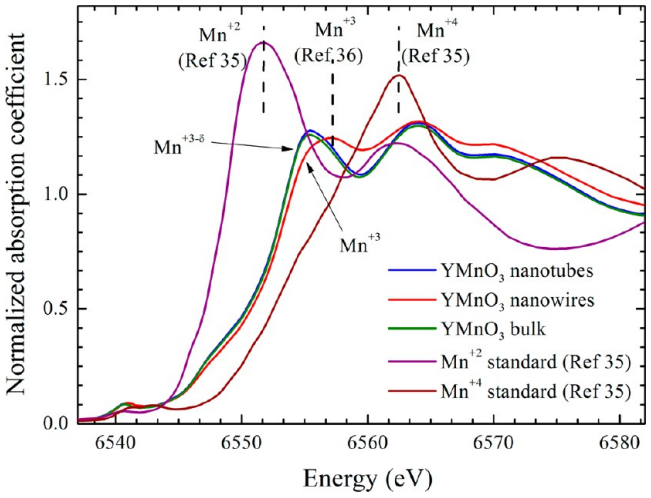


**Figure 2.** XANES spectra of templateless bulk $YMnO_3$, $YMnO_3$ nanowires, and $YMnO_3$ nanotubes as well as of standard reference compounds, including glucose−glycine−birnessite (for Mn(II)) and Δ-$MnO_2$ (for Mn(IV)).

that our as-synthesized samples possess comparable crystal structure and Mn valence.

**3.2. Size and Morphology of 1D Nanomaterials and Insights into Ferroelectricity.** The clear advantage to using template-based techniques is that the size and morphology of as-prepared products closely mimic those of the originating template architecture. As shown in Figure 3A, individual cylindrical nanowires were obtained after annealing the amorphous product isolated from a sol-loaded 200 nm PC template at 800 °C for 2 h. The polycarbonate template is expected to decompose at temperatures above 400 °C, so template residues are unlikely. Therefore, the average diameters and lengths of the resulting isolated nanowires, determined from SEM images, were measured to be 133 ± 16 nm and 5.5 ± 3 μm, respectively. The TEM image in Figure 3B highlights the smooth outer surface of a nanowire, possessing a diameter of ∼125 ± 21 nm, a finding which is consistent with the corresponding size distribution determined from SEM. Indeed, long-range crystalline ordering can be readily observed in the high-magnification TEM image, presented in Figure 3B. The SAED pattern shown in the inset of Figure 3B indicates that the nanowire sample is primarily composed of highly oriented crystalline grains. The observed spots in the electron diffraction pattern can be indexed to the −112 and 012 reflections of *h*-$YMnO_3$, respectively, confirming that the long axis of the nanowire is oriented along the [210] direction. Upon tilting the sample, we obtained high-resolution images from the region of the nanowire, as indicated by the box in Figure 3B.


dx.doi.org/10.1021/jp5068582 | J. Phys. Chem. C 2014, 118, 21695−21705

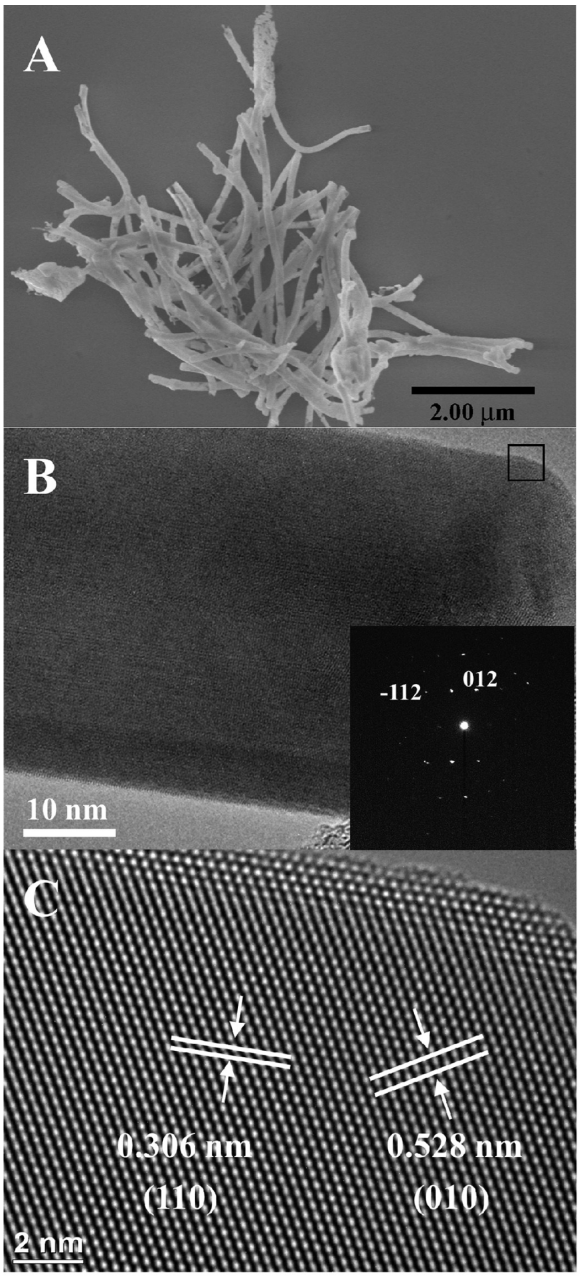


**Figure 3.** Representative SEM image of *h*-$YMnO_3$ nanowires obtained from a sol-loaded 200 nm PC template (A). A representative TEM image near the [02−1] axis is shown (B), along with a SAED pattern (inset to B) and a high-resolution image (C) taken along the [001] axis, which correspond to the region boxed off in (B).

The HRTEM images, which are representative of the sample, revealed ordered atomic columns of the material oriented along the [001] axis, with no observable dislocations or defects, indicative of their highly crystalline nature. The lattice spacings shown in Figure 3C were indexed to the (110) and (010) planes, respectively. The peaks present in the EDS spectrum (Figure S4A) validate the presence of yttrium, manganese, and oxygen with no impurity peaks. Additional peaks from the silicon substrate as well as apparent carbon impurities from within the SEM setup can be observed.

As discussed earlier, hexagonal $YMnO_3$ is known to be an improper ferroelectric at room temperature. Being a ferroelectric, the spontaneous polarization switching has been demonstrated experimentally via domain wall motion.[37] Typical nanowires have diameters of 100−200 nm, as shown in Figure 4A. An electron diffraction pattern taken from the nanowire is

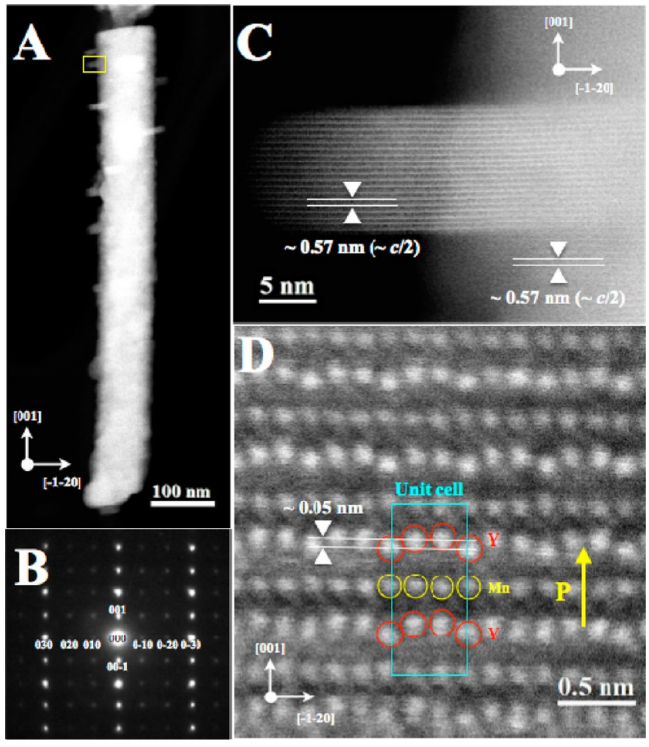


**Figure 4.** (A) A HAADF STEM image of a ∼200 nm diameter multiferroic hexagonal $YMnO_3$ nanowire. (B) An electron diffraction pattern from the nanowire shown in (A). (C) A HAADF STEM image of an epitaxial branch from the area indicated with the yellow box in (A). The *c*/2 atomic plane is continuously connected between the branch and the main body. Here, *c* represents the lattice constant along the *c*-axis. (D) An atomic resolution HAADF STEM image showing ferroelectric displacements of Y atoms. A unit cell is highlighted with a blue rectangle. Local polarization direction (*P*) is shown with the yellow arrow. The zone axis is along the [100].

shown in Figure 4B, indicating that the nanowire is high-quality and single-crystalline. The crystallographic *c*-axis is aligned with the long axis of nanowire, implying that the growth direction is mainly along the *c*-axis. However, observation of a few branches (Figure 4C) in the nanowires that are epitaxially connected with the main nanowire body suggests non-negligible growth of nanowires perpendicular to the *c*-axis. A super lattice modulation (i.e., 030 is brighter than 010 and 020) shown along the series of 010 reflections in Figure 4B strongly supports the Mn-trimerization phase transition, tripling the unit-cell volume.[38] It should be noted that the 0−10 peak corresponds to the (−1−20) plane diffraction in the real space.

In order to probe ferroelectricity, we have performed atomic resolution HAADF STEM imaging, as shown in Figure 4D. Y (red-circled) and Mn (yellow-circled) columns are only visible. The ferroelectric phase (space group $P6_3cm$) has 6 Y- and Mn-atoms and 18 O atoms in a unit cell. Y displacements about 0.05 nm along the *c*-axis are clearly visible in Figure 4D; 2/3 of Y columns in a unit cell shifted upward and 1/3 of Y columns shifted correspondingly downward, resulting in a net displacement of 1/3 Y columns upward. No noticeable displacements are found for Mn columns in Figure 4D, consistent with the previous report.[37] It is also known that there are no net O


dx.doi.org/10.1021/jp5068582 | J. Phys. Chem. C 2014, 118, 21695−21705

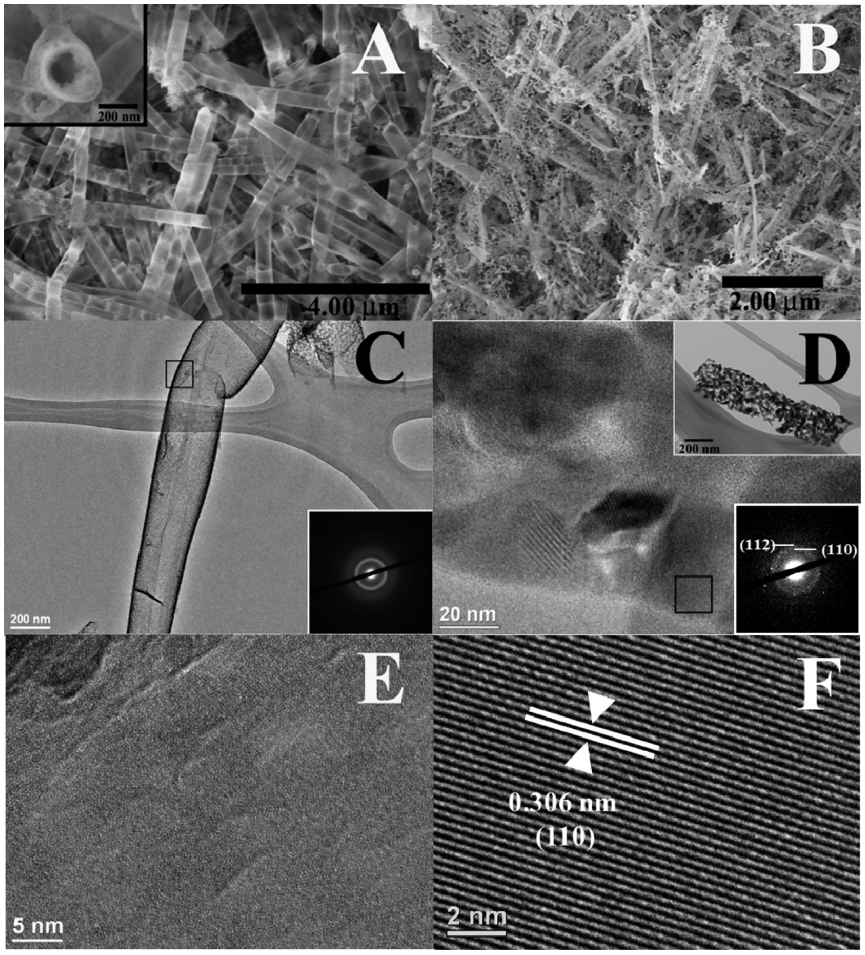


**Figure 5.** Representative SEM images of $YMnO_3$ nanotubes obtained from an AAO template after annealing at 650 °C (A) and 800 °C (B). Inset in (A) is a higher magnification image. A representative low-resolution TEM image and corresponding HRTEM image of the amorphous nanotubes prepared at 650 °C are shown in (C) and (E), respectively; the accompanying SAED pattern is evinced as an inset to (C). Low-resolution TEM and corresponding HRTEM images of the crystalline nanotubular mesh obtained after annealing at 800 °C are presented in (B) and (D), respectively, with the hollow, fractured nature of the material shown as the upper right-hand inset to (D) along with the corresponding SAED pattern (lower right-hand inset to (D)). An even higher resolution TEM image (F) from the highlighted boxed region in (D) is presented.

displacements in ferroelectric $YMnO_3$,[38] and experimentally, we do not observe any in Figure 4D. Thus, the noncentrosymmetric Y displacements (1/3 Y displacements along the *c*-axis) found in Figure 4D show that the local polarization direction is directed upward, as indicated with the yellow arrow. The atomic displacements of Y columns in Figure 4D are about 0.05 nm on average, similar to the reported value of 0.049 nm, as determined by X-ray diffraction measurements,[39] implying that the polarization value is around 5 $\mu C/cm^2$ for the $YMnO_3$ nanowires.

Interestingly, aggregated bundles of nanowires can be obtained when the amorphous product is annealed within the template itself, by contrast with the preponderance of individual nanowires which are typically isolated from the PC membrane prior to the annealing step. Apparently, the nanowires maintain their close spatial proximity to each other after the PC template has been burnt off at high temperatures, thereby allowing for the individual wires to essentially fuse together into large bundles during the crystallization process. A representative SEM image of a nanowire bundle is presented in the Supporting Information (Figure S5).

Upon utilizing AAO as the template membrane, we were unable to generate any crystalline product from the initial thermal treatment at 650 °C, as evidenced by the XRD patterns in Figure S6. Indeed, the relatively low crystallization temperature of the template material limited our ability to anneal the nanotubes within this desired structural scaffold. More specifically, raising the temperature of the muffle furnace above 650 °C would likely crystallize the alumina template into the corundum phase, which cannot be dissolved in either acid or base, thereby presenting significant problems for isolating our targeted one-dimensional nanostructures. Therefore, our first thermal treatment at 650 °C can be considered as a means of simply calcining the sol−gel precursor into a solid material, thereby facilitating the reliable isolation of the nanotubes from the template.

The nanotubes were subsequently crystallized by employing a second annealing step at 800 °C, after isolation from the template. All of the peaks present in the XRD pattern (Figure S6) obtained after annealing at 800 °C were found to correspond to the JCPDS No. 72-3594 standard for hexagonal-phase $YMnO_3$ without the presence of obvious impurities. The morphology of the nanotubes produced from AAO templates is shown in Figure 5. As depicted in Figure 5A, hollow, bamboo-like nanotubes were isolated after the initial calcination step at 650 °C. As-obtained nanotubes measured


dx.doi.org/10.1021/jp5068582 | J. Phys. Chem. C 2014, 118, 21695−21705

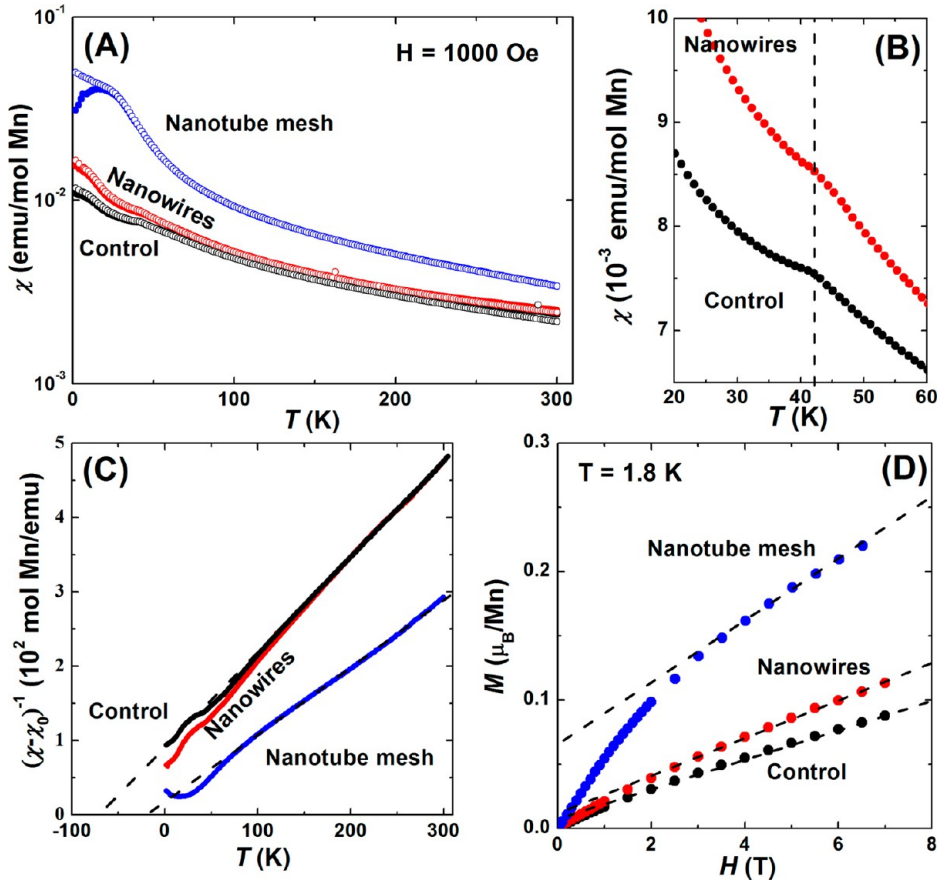


**Figure 6.** (A) Temperature dependencies of the magnetic susceptibility $\chi$ for different morphologies of $YMnO_3$: sol–gel control sample (black), nanotubular mesh (blue), and nanowires (red). FC data are shown as open circles, and ZFC data are plotted with filled circles. (B) Expanded view of the ZFC data from (A) in the vicinity of the magnetic ordering transition $T_{spin\text{-}glass}$ = 41 ± 1 K for the nanowires and the control sample (vertical dashed line). (C) Temperature dependencies of the reciprocal susceptibilities $(\chi - \chi_0)^{-1}$, which are linear with $T$. (D) Field dependencies of the magnetizations $M(H)$ measured at 1.8 K after zero field cooling. Dashed lines indicate linear contributions (see text). Color scheme is the same for panels A–D.

276 ± 52 nm in diameter and up to several microns in length. In effect, the measured diameters of the nanotubes exceeded the nominal pore dimensions of the AAO template. However, this apparent size discrepancy is not an uncommon finding and has been reported upon previously.[40−42] The pore opening of one nanotube is highlighted in the inset of Figure 5A so as to confirm the presence of the hollow core.

The corresponding TEM image shown in Figure 5C, taken after the first calcination step at 650 °C, confirms the nanotubular structural motif, as evidenced by contrast differences between the center and the sidewalls. The bamboo-like morphology of these nanotubes has been previously noted in similar template-mediated sol–gel syntheses using AAO.[43] The disordered atomic structure in the high-resolution TEM image of the nanotube shown in Figure 5E, coupled with the relatively diffuse SAED pattern (inset to Figure 5C), substantiate our conclusion that the nanotubes isolated after initially heating to 650 °C were in fact amorphous, an observation consistent with the XRD data (Figure S6).

However, after annealing to 800 °C, the fragile walls of the nanotubes collapsed to produce relatively fragmented and broken up structures (Figure 5B), which we designate as a nanotubular mesh. The fractured nature of the material was confirmed by TEM, as shown in the upper right-hand inset to Figure 5D. Interestingly, the average size of the individual constituent nanosized grains that make up the nanotubular mesh was measured to be 17 ± 3.5 nm. The high-resolution TEM image, shown in Figure 5D, indicated that these individual grains are indeed crystalline. Meanwhile, the high-resolution TEM image, presented in Figure 5F and taken at even higher magnification from a localized region in Figure 5D, reveals the presence of lattice planes of a representative crystallite with a measured atomic spacing of about 0.306 nm, which has been assigned to the (110) plane of $h$-$YMnO_3$.

The nontrivial SAED pattern in the lower right-hand inset of Figure 5D is consistent with an overall polycrystalline structure for the nanotubular mesh. Nevertheless, the observed rings in the electron diffraction pattern can be indexed to the expected 112 and 110 reflections, respectively, of $h$-$YMnO_3$. Taken together, these data suggest that we can reasonably expect that the physicochemical properties exhibited by our nanotubular mesh will more likely resemble that of its basic building blocks, i.e., small constituent nanoparticles, as compared with a true discrete, single-crystalline one-dimensional structure possessing a diameter of ∼275 nm. Elemental analysis by EDS is also shown in the Supporting Information (Figure S4B), thereby confirming the inherent purity of the crystallized nanotube sample.

**3.3. Insights into Mechanism of Formation.** The key driving force for the sol to fill in the various templates appeared to be through the application of external forces such as either the use of a syringe or vacuum, and was aided by capillary


dx.doi.org/10.1021/jp5068582 | J. Phys. Chem. C 2014, 118, 21695−21705

action in the presence of relatively polar solvents. Hence, as both templates tested were hydrophilic, the correlation of the template material utilized with the resulting product morphology observed in our work is actually consistent with previous reports.[44] For example, in the case of nanowire formation within a polymeric PC membrane, the sol likely completely fills and saturates the interior of the pores of the template, thereby yielding, after activating the gel by thermal drying, a solid one-dimensional structure which mimics and mirrors the cylindrical shape of the channels from whence it was derived. Subsequently, the aggregation and fusion of precursor particles during the calcination process produces a solid nanowire. Although the average diameter of our nanowires is slightly smaller than the reported nominal pore size of the template, this result has also been explained previously for template-mediated sol−gel syntheses.[44−46] Specifically, during the drying and annealing process, the amorphous one-dimensional sol−gel product shrinks to some extent, due to densification, thereby yielding a final product possessing a diameter that is slightly smaller than that of the originating pores.

By contrast, the nanotube morphology is most commonly associated with the use of AAO membranes in template-mediated sol−gel syntheses.[27,43−49] In general, it is considered that the formation of hollow nanotubes, as opposed to filled nanowires, can be attributed to a strong interaction between the sol particles and the pore walls of the template membrane, which is more favorable than sol−sol particulate interactions. As a result, heterogeneous nucleation and growth can occur under these conditions. Another hypothesis[43] claims that oxide nanotubes are favored to form in AAO templates because the porous AAO pore walls inherently possess large amounts of structural defect sites, which would locally facilitate the nucleation of sol particles, thereby ultimately leading to tube production. Interestingly, the formation of either straight or bamboo-like nanotubes may depend on the viscosity of the sol, a factor which has an impact on gel formation. Specifically, it is postulated that the formation of bamboo-like motifs is associated with a concomitant release of gas bubbles during the calcination step.

Moreover, the nature of the metal oxide template allows for electrostatic interactions to play a significant role in subsequent nanostructure growth.[27,46,47,49] For example, as in the analogous formation of $LaCoO_3$ nanostructures under the slightly acidic experimental conditions (pH ∼ 6−7), it was proposed[27] that weakly positively charged sol particles interacted with anionic sites on the alumina pore wall, thereby resulting in preferential adsorption and wetting of sol particles along the pore surfaces. Subsequent thermal calcination in our case would therefore have yielded nanotubes. It is worth noting that neither increasing the sol concentration nor increasing the number of times the sol was loaded into an AAO template resulted in nanowire formation. Our data are consistent with prior observations on the analogous formation of $PbTiO_3$ nanotubes and nanowires.[44]

**3.4. Magnetic Characterization.** The magnetic properties of our nanostructures are presented in Figure 6, along with the characterization of a templateless control sample, grown via the sol−gel process, for comparison. Figure 6A displays the temperature dependencies of the magnetic susceptibilities, $\chi = M/H$, for which the samples were cooled either with an applied external field ($H$) of 1000 Oe (FC) or with zero field (ZFC). Measurements were carried out upon warming with $H$ = 1000 Oe and were normalized by the nominal composition of $YMnO_3$. In all cases, $\chi$ was found to decrease as the temperature was raised, indicating the presence of magnetic moments.

While the magnetic susceptibilities, $\chi$, of the nanowire and control samples are remarkably similar, we found that the crystalline nanotubular mesh gave rise to slightly enhanced $\chi$ values across nearly the entire temperature range as well as to a more pronounced feature at the ordering transition temperature than in the control sample. Indeed, it was only in this sol−gel nanotube sample that we observed, upon field cooling, a clear enhancement in $\chi$ within the ordered state, indicating the onset of a very slight FC−ZFC hysteresis.

As shown in Figure 6B, we observe a broad cusp in $\chi$ at 41 ± 1 K for both the nanowires and the templateless control sample that we interpret as the manifestation of a spin-glass transition. This assertion is consistent with prior observations of comparable hexagonal $YMnO_3$ structures.[50−52] We likewise construe the broad maximum observed in the nanotube mesh sample at which the FC and ZFC data diverge (Figure 6A) as the onset of a spin-glass transition at 26 ± 3 K. We take these results to suggest that all three samples, including the purportedly bulk templateless control sample, are ultimately composed of particles or grains with a nanosized length scale. For such nanoscale antiferromagnets, the magnetic contributions emanating from surface spins become increasingly important due to the increased surface area-to-volume ratios in these systems.

We have directly observed that our templateless bulk control samples were polycrystalline and consist of many nanoscale crystalline constituent grains, as shown in a higher magnification SEM image (Figure S7). The average diameter of these particulate grains that comprised the surface of the bulk control was measured to be 113 ± 23 nm with the average constituent crystallite size of the "bulk" aggregate noted to be 39 nm, based on XRD diffraction data. Concurrent with our observed magnetic data, we suggest that the preparation of our ostensible control sample, which was the result of annealing our sol−gel precursor in the absence of any templating manifold, yielded a material that was actually partially composed of nanosized grains. Therefore, the observation of the spin-glass transition temperature may have been due in part to the chemical nature of the sol−gel process, as opposed to being wholly a function of the physical morphological constraints imposed by the presence of the template. Nevertheless, our magnetic measurements of the nanotubular mesh sample suggest that the magnetic properties of 1D $YMnO_3$ can be modified to some extent by nuanced alterations in its structural motif.

Plots of reciprocal susceptibility and magnetic isotherms provide further details into the differences manifested by the nanotubular mesh. The temperature dependence of the corrected reciprocal susceptibility $(\chi - \chi_0)^{-1}$ is shown in Figure 6C for each sample, measured under ZFC conditions, wherein $\chi_0$ represents the temperature-independent contribution to $\chi$. We observe that $(\chi - \chi_0)^{-1}$ is linear above $\sim T_{\text{spin-glass}}$, an indication of Curie−Weiss-like behavior, from which an effective moment of 2.5(1) $\mu_B$/Mn can be extracted for the nanowires and the control sample. The nanotubular mesh, however, possesses a slightly larger moment of 3.0(1) $\mu_B$/Mn. Figure 6D highlights the ZFC magnetic isotherms of each sample at $T$ = 1.8 K. In each case, the magnetization, $M$, can be described by a component that saturates with $H$ and one that is linear in $H$. Although the linear component of $M$ is modestly larger for the nanotubes than for the other morphologies, it


dx.doi.org/10.1021/jp5068582 | J. Phys. Chem. C 2014, 118, 21695−21705

appears to be the saturating component from which the majority of the observable enhancement in $\chi$ stems. The origin of the linear or nonsaturating part of the magnetization may result either from the continuous break down of sublattice pairing or from the presence of uncompensated spins, perhaps on the surface of the nanotubes.[51]

Collectively, the polycrystalline nanotubular mesh (i.e., grain size of 17 ± 3.5 nm) exhibits a pronounced lower spin-glass transition temperature at ∼26 ± 3 K as well as a modest increase in $\chi$ within the ordered state after field cooling as compared with both nanowire and bulk control samples. These results are somewhat interesting, since all the samples appear to possess comparable Mn oxidation states in the $YMnO_3$ structure, as confirmed by XANES. The lower spin glass transition temperature associated with the nanotubular mesh can likely be ascribed to the substantially smaller constituent crystallite size of this sample (∼14 nm) as compared with analogous values associated with both templateless bulk control and nanowire samples (∼37 and ∼39 nm), as determined from XRD data.

The key additional implications of our assertion that the smaller crystallite size accounts for the magnetic behavior observed for the nanotubular mesh would be that the surface-to-volume ratio of each constituent nanograin is correspondingly increased, thereby increasing the fraction of moments that are uncompensated along the surfaces of the particle. Such a configuration could be expected to yield a lower spin-glass transition temperature and a larger resulting magnetic moment. According to the phenomenological scaling relation between crystallite size and magnetic ordering temperature, as suggested by prior reports,[53,54] the magnetic transition temperature scales linearly with crystallite size and inversely with volume in the nanoscale region. Furthermore, this relationship is consistent with previous measurements and observations associated with various other magnetic nanomaterials including but not limited to $BiFeO_3$, NiO, and $MnFeO_4$.[55−58]

**3.5. Infrared Spectroscopy.** Our as-synthesized nanomaterials were also investigated with FTIR spectroscopy by comparison with our templateless control sample of $YMnO_3$ (Figure 7) within the far IR region (700−200 $cm^{-1}$). We found that the spectra for all samples, including the templateless bulk control, were consistent with previous results from the literature.[16,17] While all discernible peaks can be assigned to the expected lines of $A_1$ and $E_1$ symmetry, we observed some small differences in the region between 350 and 500 $cm^{-1}$. Specifically, the peaks in this region appear to be significantly broadened. While the feature at ∼380 $cm^{-1}$, corresponding to a vibrational mode of $A_1$ symmetry, is present, other vibrational modes located at 430, 454, 498, and 511 $cm^{-1}$, which have been observed in previous reports,[18,19] are either notably absent or strongly attenuated in our as-prepared samples. We speculate that these differences may ultimately be attributed to either nanoscale strain effects or to differences in crystal structures, namely the particular space group associated with our as-prepared $YMnO_3$ samples. Although our as-synthesized products are all hexagonal in nature, finite and nuanced differences in bond arrangement and configuration, associated with the templateless bulk, nanotube, and nanowire samples, respectively, may be more dramatically enhanced in the far-IR region.

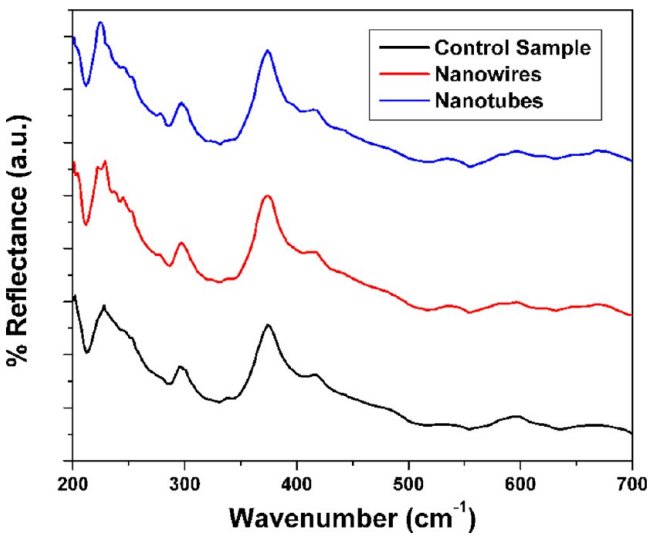


**Figure 7.** FT-IR spectra of our as-prepared $YMnO_3$ samples, namely a nanotubular mesh (blue), nanowires (red), and a control sample prepared from our sol−gel precursor (black).

## 4. CONCLUSIONS

The current article therefore represents an important contribution toward broadening the synthesis of one-dimensional yttrium manganese oxides. We have shown that the template-mediated sol−gel synthesis of $YMnO_3$ could be successfully employed to produce phase-pure 1D nanostructures. Of interest, the chemistry of the template pore wall appeared to affect the nucleation of the sol, which resulted in the production of both nanowires and nanotubes. In effect, amorphous nanostructures were typically isolated from the template membrane prior to a subsequent thermal treatment in order to generate one-dimensional nanostructures of phase-pure crystalline *h*-$YMnO_3$.

Although the nanowires maintained their solid structure after the annealing step, the morphology of the nanotubes altered into that of a nanotubular mesh, possessing a particulate grain size of 17 ± 3.5 nm. Average diameters and lengths of the crystalline nanowires were measured to be 125 ± 21 nm and 5.5 ± 3 $\mu$m, respectively, suggesting a slight contraction of the material upon annealing. HRTEM and SAED analysis revealed that the nanowires were highly crystalline with long-range atomic ordering, whereas the nanotubular mesh was composed of highly crystalline grains, bearing an overall polycrystalline structure. More specifically, with respect to nanowires, the associated electron diffraction pattern suggests that these nanowires are not only high quality but also single crystalline; the crystallographic *c*-axis is aligned with the long axis of nanowire, implying that the growth direction is mainly along the *c*-axis. Moreover, we provide convincing evidence for the presence of ferroelectric behavior within as-prepared individual nanowires, which had not been previously observed in these structural motifs.

Furthermore, on the basis of EXAFS and XANES experiments, we concluded that the formal oxidation state of Mn in our all three samples is essentially +3. Moreover, we found that the crystal structure is not significantly dependent upon the actual morphology of $YMnO_3$ (e.g., nanowires versus nanotubes versus bulk control samples) and that, overall, our as-synthesized samples possess comparable crystal structure and Mn valence.

Optical measurements (i.e., far-IR) evinced behavior similar to that for bulk $YMnO_3$. Magnetic characterization demon-


dx.doi.org/10.1021/jp5068582 | J. Phys. Chem. C 2014, 118, 21695−21705

strated that our $YMnO_3$ templateless bulk control and nanowire samples manifested a spin-glass transition at 41 ± 1 K, which is consistent with what has been nominally reported for $YMnO_3$ nanoparticles, whereas the onset of a spin-glass transition associated with the nanotubular mesh was noted to be slightly lower at 26 ± 3 K, an observation which could be attributed to its substantially smaller constituent crystallite size (i.e., ∼14 nm) as compared with the other analogous samples tested (i.e., ∼37 and 39 nm).

Since even our control sample demonstrated overall comparable magnetic behavior with those of our samples, it is proposed that the observed spin-glass transition was due in part to chemical nuances associated with the sol−gel process itself and could not be ascribed entirely to the intrinsic physical morphology induced by the template. Additional investigation by SEM showed that our control sample does indeed exhibit a nanosized granular texture. Both the control sample and the nanowires evinced magnetic moments of 2.5 $\mu_B$/Mn. By contrast, our sol−gel-generated nanotubular mesh yielded a magnetic moment of 3.0 $\mu_B$/Mn, which could be potentially attributed to the presence of a larger fraction of uncompensated surface spins, likely a consequence of the smaller crystallite size.

Together, our results not only exemplify the successful application of a template-mediated sol−gel synthesis for the production of 1-D *h*-$YMnO_3$ nanostructures but also illustrate the principle that the magnetic properties of a material can be modified to some extent by varying its structural morphology. Future work will focus on correlating 1D size (i.e., diameter) with the corresponding physicochemical properties of these materials.

## ■ ASSOCIATED CONTENT

### Supporting Information

Additional crystal structures as well as structural characterization data (including XAFS analysis, EDAX, SEM, and XRD analyses) of the nanowires. This material is available free of charge via the Internet at http://pubs.acs.org.

## ■ AUTHOR INFORMATION

### Corresponding Author

*E-mail: sswong@bnl.gov, stanislaus.wong@stonybrook.edu (S.S.W.).

### Notes

The authors declare no competing financial interest.

## ■ ACKNOWLEDGMENTS

We thank Jim Quinn and Susan Van Horn for their assistance with electron microscopy and energy dispersive X-ray spectroscopy. Funds for research work (including support for J.M.P., J.H., A.L.T., H.L., M.H., J.W.S., A.C.S., M.C.A., Y.Z., and S.S.W.) at Brookhaven National Laboratory (BNL) were provided by the U.S. Department of Energy, Office of Basic Energy Sciences, Materials Sciences and Engineering Division, under Contract DE-AC02-98CH10886. A.I.F. acknowledges support of the Department of Energy Grant DE-FG02-03ER15476. Beamlines X18A and X19A at the NSLS are supported in part by the Synchrotron Catalysis Consortium, U.S. Department of Energy Grant DE-FG02-05ER15688. High-resolution electron microscopy data in this article were collected in part at BNL's Center for Functional Nanomaterials, which is also supported by the U.S. Department of Energy under Contract DE-AC02-98CH10886.

## ■ REFERENCES

(1) Eerenstein, W.; Mathur, N. D.; Scott, J. F. Multiferroic and Magnetoelectric Materials. *Nature* **2006**, *442*, 759−765.

(2) Kim, K.-T.; Kim, C.-I. The Effects of Drying Temperature on the Crystallization of $YMnO_3$ Thin Films Prepared by Sol-Gel Method Using Alkoxides. *J. Eur. Ceram. Soc.* **2004**, *24*, 2613−2617.

(3) Samal, S. L.; Green, W.; Lofland, S. E.; Ramanujachary, K. V.; Das, D.; Ganguli, A. K. Study on the Solid Solution of $YMn_{1-x}Fe_xO_3$: Structural, Magnetic and Dielectric Properties. *J. Solid State Chem.* **2008**, *181*, 61−66.

(4) Park, T.-J.; Mao, Y.; Wong, S. S. Synthesis and Characterization of Multiferroic $BiFeO_3$ Nanotubes. *Chem. Commun.* **2004**, *23*, 2708−2709.

(5) Park, T.-J.; Papaefthymiou, G. C.; Viescas, A. J.; Moodenbaugh, A. R.; Wong, S. S. Size-Dependent Magnetic Properties of Single-Crystalline Multiferroic $BiFeO_3$ Nanoparticles. *Nano Lett.* **2007**, *7*, 766−772.

(6) Ramesh, R.; Spaldin, N. A. Multiferroics: Progress and Prospects in Thin Films. *Nat. Mater.* **2007**, *6*, 21−29.

(7) Sekhar, M. C.; Prasad, N. V. Dielectric, Impedance, Magnetic and Magnetoelectric Measurements on $YMnO_3$. *Ferroelectrics* **2006**, *345*, 45−57.

(8) Fujimura, N.; Azuma, S.-i.; Aoki, N.; Yoshimura, T.; Ito, T. Growth Mechanism of $YMnO_3$ Film as a New Candidate for Nonvolatile Memory Devices. *J. Appl. Phys.* **1996**, *80*, 7084−7088.

(9) Ismailzade, I. G.; Kizhaev, S. A. Determination of the Curie Point of the Ferroelectrics $YMnO_3$ and $YbMnO_3$. *Sov. Phys. Solid State* **1965**, *7*, 236−238.

(10) Qian, M.; Dong, J.; Zheng, Q. Electronic Structure of the Ferroelectromagnet $YMnO_3$. *Phys. Lett. A* **2000**, *270*, 96−101.

(11) Teowee, G.; McCarthy, K. C.; McCarthy, F. S.; Bukowski, T. J.; Davis, D. G.; Uhlmann, D. R. Dielectric and Ferroelectric Properties of Sol-Gel Derived $YMnO_3$ Films. *J. Sol-Gel Sci. Technol.* **1998**, *13*, 899−902.

(12) Yakel, H. L.; Koehler, W. C.; Bertaut, E. F.; Forrat, E. F. On the Crystal Structure of the Manganese(III) Trioxides of the Heavy Lanthanides and Yttrium. *Acta Crystallogr.* **1963**, *16*, 957−962.

(13) Zhou, J. S.; Goodenough, J. B.; Gallardo-Amores, J. M.; Morán, E.; Alario-Franco, M. A.; Caudillo, R. Hexagonal versus Perovskite Phase of Manganite $RMnO_3$ (R = Y, Ho, Er, Tm, Yb, Lu). *Phys. Rev. B* **2006**, *74*, 014422/1−7.

(14) Stampler, E. S.; Sheets, W. C.; Prellier, W.; Marks, T. J.; Poeppelmeier, K. R. Hydrothermal Synthesis of $LnMnO_3$ (Ln = Ho-Lu and Y): Exploiting Amphoterism in Late Rare-Earth Oxides. *J. Mater. Chem.* **2009**, *19*, 4375−4381.

(15) Smith, A. E.; Mizoguchi, H.; Delaney, K.; Spaldin, N. A.; Sleight, A. W.; Subramanian, M. A. $Mn^{3+}$ in Trigonal Bipyramidal Coordination: A New Blue Chromophore. *J. Am. Chem. Soc.* **2009**, *131*, 17084−17086.

(16) Kim, S. H.; Lee, S. H.; Kim, T. H.; Zyung, T.; Jeong, Y. H.; Jang, M. S. Growth, Ferroelectric Properties, and Phonon Modes of $YMnO_3$ Single Crystal. *Cryst. Res. Technol.* **2000**, *35*, 19−27.

(17) Iliev, M. N.; Lee, H. G.; Popov, V. N.; Abrashev, M. V.; Hamed, A.; Meng, R. L.; Chu, C. W. Raman- and Infrared-Active Phonons in Hexagonal $YMnO_3$: Experiment and Lattice-Dynamical Calculations. *Phys. Rev. B* **1997**, *56*, 2488−2494.

(18) Fukumura, H.; Matsui, S.; Harima, H.; Kisoda, K.; Takahashi, T.; Yoshimura, T.; Fujimura, N. Raman Scattering Studies on Multiferroic $YMnO_3$. *J. Phys.: Condens. Matter* **2007**, *19*, 365239/1−9.

(19) Kück, S.; Hartung, S.; Hurling, S.; Petermann, K.; Huber, G. Optical Transitions in $Mn^{3+}$-Doped Garnets. *Phys. Rev. B* **1998**, *57*, 2203−2216.

(20) Ye, Y.; Fan, H.; Li, J. Fabrication and Texture Evolution of Hexagonal $YMnO_3$ Nanofibers by Electrospinning. *Mater. Lett.* **2010**, *64*, 419−421.

(21) Zapata, J.; Narvaez, J.; Lopera, W.; Gomez, M. E.; Mendoza, G. A.; Prieto, P. Electric and Magnetic Properties of Multiferroic $BiFeO_3$ and $YMnO_3$ Thin Films. *IEEE Trans. Magn.* **2008**, *44*, 2895−2898.

(22) Balasubramanian, K. R.; Chang, K.-C.; Mohammad, F. A.; Porter, L. M.; Salvador, P. A.; DiMaio, J.; Davis, R. F. Growth and Structural Investigations of Epitaxial Hexagonal $YMnO_3$ Thin Films Deposited on Wurtzite GaN(001) Substrates. *Thin Solid Films* **2006**, *515*, 1807−1813.
(23) do Nascimento, G. M.; Hou, T.; Kim, Y. A.; Muramatsu, H.; Hayashi, T.; Endo, M.; Akuzawa, N.; Dresselhaus, M. S. Comparison of the Resonance Raman Behavior of Double-Walled Carbon Nanotubes Doped with Bromine or Iodine Vapors. *J. Phys. Chem. C* **2009**, *113*, 3934−3938.
(24) Chen, Z.; Ma, C.-L.; Wu, F.-X.; Chen, Y. B.; Zhou, J.; Yuan, G.-L.; Gu, Z.-B.; Zhang, S.-T.; Chen, Y.-F. The Electrical and Magnetic Properties of Epitaxial Orthorhombic $YMnO_3$ Thin Films Grown under Various Oxygen Pressures. *Appl. Surf. Sci.* **2011**, *257*, 8033−8037.
(25) Liu, S.-H.; Huang, J.-C.-A.; Qi, X.; Lin, W.-J.; Siao, Y.-J.; Lin, C.-R.; Chen, J.-M.; Tang, M.-T.; Lee, Y.-H.; Lee, J.-C. Structural Transformation and Charge Transfer Induced Ferroelectricity and Magnetism in Annealed $YMnO_3$. *AIP Adv.* **2011**, *1*, 032173/1−11.
(26) Santulli, A. C.; Feygenson, M.; Camino, F. E.; Aronson, M. C.; Wong, S. S. Synthesis and Characterization of One-Dimensional $Cr_2O_3$ Nanostructures. *Chem. Mater.* **2011**, *23*, 1000−1008.
(27) Yang, Z.; Huang, Y.; Dong, B.; Li, H. L.; Shi, S. Q. Sol−Gel Template Synthesis and Characterization of $LaCoO_3$ Nanowires. *Appl. Phys. A: Mater. Sci. Process.* **2006**, *84*, 117−122.
(28) Yang, Z.; Huang, Y.; Dong, B.; Li, H.-L. Template Induced Sol-Gel Synthesis of Highly Ordered $LaNiO_3$ Nanowires. *J. Solid State Chem.* **2005**, *178*, 1157−1164.
(29) Uusi-Esko, K.; Malm, J.; Karppinen, M. Atomic Layer Deposition of Hexagonal and Orthorhombic $YMnO_3$ Thin Films. *Chem. Mater.* **2009**, *21*, 5691−5694.
(30) Uusi-Esko, K.; Malm, J.; Imamura, N.; Yamauchi, H.; Karppinen, M. Characterization of $RMnO_3$ (R = Sc, Y, Dy-Lu): High-Pressure Synthesized Metastable Perovskites and Their Hexagonal Precursor Phases. *Mater. Chem. Phys.* **2008**, *112*, 1029−1034.
(31) Salvador, P. A.; Doan, T.-D.; Mercey, B.; Raveau, B. Stabilization of $YMnO_3$ in a Perovskite Structure as a Thin Film. *Chem. Mater.* **1998**, *10*, 2592−2595.
(32) Brinks, H. W.; Fjellvåg, H.; Kjekshus, A. Synthesis of Metastable Perovskite-Type $YMnO_3$ and $HoMnO_3$. *J. Solid State Chem.* **1997**, *129*, 334−340.
(33) Łukaszewicz, K.; Karut-Kalicińska, J. X-Ray Investigations of the Crystal Structure and Phase Transitions of $YMnO_3$. *Ferroelectrics* **1974**, *7*, 81−82.
(34) Katsufuji, T.; Masaki, M.; Machida, A.; Moritomo, M.; Kato, K.; Nishibori, E.; Takata, M.; Sakata, M.; Ohoyama, K.; Kitazawa, K.; Takagi, H. Crystal Structure and Magnetic Properties of Hexagonal $RMnO_3$ (R = Y, Lu, and Sc) and the Effect of Doping. *Phys. Rev. B* **2002**, *66*, 134434/1−8.
(35) Jokic, A.; Frenkel, A. I.; Vairavamurthy, M. A.; Huang, P. M. Birnessite Catalysis of the Maillard Reaction: Its Significance in Natural Humification. *Geophys. Res. Lett.* **2001**, *28*, 3899−3902.
(36) Jokic, A.; Wang, M. C.; Liu, C.; Frenkel, A. I.; Huang, P. M. Integration of the Polyphenol and Maillard Reactions into a Unified Abiotic Pathway for Humification in Nature: The Role of $\delta$-$MnO_2$. *Org. Geochem.* **2004**, *35*, 747−762.
(37) Han, M.-G.; Zhu, Y.; Wu, L.; Aoki, T.; Volkov, V.; Wang, X.; Chae, S. C.; Oh, Y. S.; Cheong, S.-W. Ferroelectric Switching Dynamics of Topological Vortex Domains in a Hexagonal Manganite. *Adv. Mater.* **2013**, *25*, 2415−2421.
(38) Van Aken, B. B.; Palstra, T. M.; Filippetti, A.; Spaldin, N. A. The Origin of Ferroelectricity in Magnetoelectric $YMnO_3$. *Nat. Mater.* **2004**, *3*, 164−170.
(39) Van Aken, B. B.; Meetsma, A.; Palstra, T. T. M. Hexagonal $YMnO_3$. *Acta Crystallogr., Sect. E* **2001**, *C57*, 230−232.
(40) Schönenberger, C.; van der Zande, B. M. I.; Fokkink, L. G. J.; Henny, M.; Schmid, C.; Krüger, M.; Bachtold, A.; Huber, R.; Birk, H.; Staufer, U. Template Synthesis of Nanowires in Porous Polycarbonate Membranes: Electrochemistry and Morphology. *J. Phys. Chem. B* **1997**, *101*, 5497−5505.
(41) Koenigsmann, C.; Santulli, A. C.; Sutter, E.; Wong, S. S. Ambient Surfactantless Synthesis, Growth Mechanism, and Size-Dependent Electrocatalytic Behavior of High-Quality, Single Crystalline Palladium Nanowires. *ACS Nano* **2011**, *5*, 7471−7487.
(42) Koenigsmann, C.; Sutter, E.; Chiesa, T. A.; Adzic, R. R.; Wong, S. S. Highly Enhanced Electrocatalytic Oxygen Reduction Performance Observed in Bimetallic Palladium-Based Nanowires Prepared under Ambient, Surfactantless Conditions. *Nano Lett.* **2012**, *12*, 2013−2020.
(43) Kuang, Q.; Lin, Z.-W.; Lian, W.; Jiang, Z.-Y.; Xie, Z.-X.; Huang, R.-B.; Zheng, L.-S. Syntheses of Rare-Earth Metal Oxide Nanotubes by the Sol−Gel Method Assisted with Porous Anodic Aluminum Oxide Templates. *J. Solid State Chem.* **2007**, *180*, 1236−1242.
(44) Hernandez-Sanchez, B. A.; Chang, K.-S.; Scancella, M. T.; Burris, J. L.; Kohli, S.; Fisher, E. R.; Dorhout, P. K. Examination of Size-Induced Ferroelectric Phase Transitions in Template Synthesized $PbTiO_3$ Nanotubes and Nanofibers. *Chem. Mater.* **2005**, *17*, 5909−5919.
(45) Singh, S.; Krupanidhi, S. B. Synthesis, Structural Characterization and Ferroelectric Properties of $Pb_{0.76}Ca_{0.24}TiO_3$ Nanotubes. *Mater. Chem. Phys.* **2011**, *131*, 443−448.
(46) Zhu, W.; Wang, W.; Xu, H.; Shi, J. Fabrication of Ordered $SnO_2$ Nanotube Arrays via a Template Route. *Mater. Chem. Phys.* **2006**, *99*, 127−130.
(47) Wu, G. S.; Xie, T.; Yuan, X. Y.; Li, Y.; Yang, L.; Xiao, Y. H.; Zhang, L. D. Controlled Synthesis of ZnO Nanowires or Nanotubes via Sol−Gel Template Process. *Solid State Commun.* **2005**, *134*, 485−489.
(48) Wang, W.; Ke, H.; Rao, J.; Feng, J.; Feng, M.; Jia, D.; Zhou, Y. Sol-Gel Synthesis of $Bi_{3.25}La_{0.75}Ti_3O_{12}$ Nanotubes. *J. Alloys Compd.* **2011**, *509*, 4722−4725.
(49) Wu, G.; Zhang, L.; Cheng, B.; Xie, T.; Yuan, X. Synthesis of $Eu_2O_3$ Nanotube Arrays through a Facile Sol-Gel Template Approach. *J. Am. Chem. Soc.* **2004**, *126*, 5976−5977.
(50) Chen, W. R.; Zhang, F. C.; Miao, J.; Xu, B.; Cao, L. X.; Qiu, X. G.; Zhao, B. R. Magnetic Properties of the Self-Doped Yttrium Manganites $YMn_{1+x}O_3$. *J. Phys.: Condens. Matter* **2005**, *17*, 8029−8036.
(51) Zheng, H. W.; Liu, Y. F.; Zhang, W. Y.; Liu, S. J.; Zhang, H. R.; Wang, K. F. Spin-Glassy Behavior and Exchange Bias Effect of Hexagonal $YMnO_3$ Nanoparticles Fabricated by Hydrothermal Process. *J. Appl. Phys.* **2010**, *107*, 053901/1−4.
(52) Huang, X. H.; Ding, J. F.; Zhang, G. Q.; Hou, Y.; Yao, Y. P.; Li, X. G. Size-Dependent Exchange Bias in $La_{0.25}Ca_{0.75}MnO_3$ Nanoparticles. *Phys. Rev. B* **2008**, *78*, 224408/1−5.
(53) Landau, D. P. Finite-Size Behavior of the Simple-Cubic Ising Lattice. *Phys. Rev. B* **1976**, *14*, 255−262.
(54) Batlle, X.; Labarta, A. Finite-Size Effects in Fine Particles: Magnetic and Transport Properties. *J. Phys. D: Appl. Phys.* **2002**, *35*, R15−R42.
(55) Han, T.-C.; Hsu, W.-L.; Lee, W.-D. Grain Size-Dependent Magnetic and Electric Properties in Nanosized $YMnO_3$ Multiferroic Ceramics. *Nanoscale Res. Lett.* **2011**, *6*, 1−8.
(56) Selbach, S. M.; Tybell, T.; Einarsrud, M.-A.; Grande, T. Size-Dependent Properties of Multiferroic $BiFeO_3$ Nanoparticles. *Chem. Mater.* **2007**, *19*, 6478−6484.
(57) Yi, J.; Ding, J.; Feng, Y.; Peng, G.; Chow, G.; Kawazoe, Y.; Liu, B.; Yin, J.; Thongmee, S. Size-Dependent Magnetism and Spin-Glass Behavior of Amorphous NiO Bulk, Clusters, and Nanocrystals: Experiments and First-Principles Calculations. *Phys. Rev. B* **2007**, *76*, 224402/1−5.
(58) Chen, J. P.; Sorensen, C. M.; Klabunde, K. J.; Hadjipanayis, G. C.; Devlin, E.; Kostikas, A. Size-Dependent Magnetic Properties of $MnFe_2O_4$ Fine Particles Synthesized by Coprecipitation. *Phys. Rev. B* **1996**, *54*, 9288−9296.